Interplay between destructive quantum interference and symmetry-breaking phenomena in graphene quantum junctions

Interplay between destructive quantum interference and symmetry-breaking phenomena in graphene quantum junctions

A. Valli,[1] A. Amaricci,[1] V. Brosco,[1,2] and M. Capone[1]
[1] *Scuola Internazionale Superiore di Studi Avanzati (SISSA), and CNR-IOM Democritos, Istituto Officina dei Materiali, Consiglio Nazionale delle Ricerche, Via Bonomea 265, 34136 Trieste, Italy and*
[2] *ISC-CNR and Department of Physics, Sapienza University of Rome, P.le A. Moro 5, 00185 Rome, Italy*
(Dated: August 21, 2019)

We study the role of electronic spin and valley symmetry in the quantum interference (QI) patterns of the transmission function in graphene quantum junctions. In particular, we link it to the position of the destructive QI anti-resonances. When the spin or valley symmetry is preserved, electrons with opposite spin or valley display the same interference pattern. On the other hand, when a symmetry is lifted the anti-resonances are split, with a consequent dramatic differentiation of the transport properties in the respective channel. We demonstrate rigorously this link in terms of the analytical structure of the electronic Green function which follows from the symmetries of the microscopic model and we confirm the result with numerical calculations for graphene nanoflakes. We argue that this is a generic and robust feature that can be exploited in different ways for the realization of nanoelectronic QI devices, generalizing the recent proposal of a QI-assisted spin-filtering effect [A. Valli et al. Nano Lett. **18**, 2158 (2018)].

I. INTRODUCTION

Quantum-interference (QI) effects in the electron transport in nanostructures are a direct evidence of the particle-wave duality of electrons, which is deeply rooted in the fundamentals of quantum mechanics. From a theoretical point of view, it is well established that ballistic electron transport in molecular junctions characterized by multiple transmission paths displays clear signatures of QI. The prototype of completely destructive QI is the *meta*-benzene molecular junction.[1–3] In the *classical* interpretation, QI emerges when electrons propagating through two different spatial paths along the short- and the long-arms of the ring acquire a phase difference $\Delta\phi = \pi$,[2,3] yielding a complete cancellation of the transmitted wave amplitude. Interestingly, this view was recently challenged[4] in favor of a different interpretation, where the antiresonance is a consequence of interference in energy space between different molecular orbitals. Independently of its origin, the presence of a QI antiresonance close to the Fermi level drastically influences the transport properties of quantum junctions and results in huge ON/OFF ratios, which can be exploited for the realization of transistors[2,3] or spin filters,[5–9] nanocircuitry,[10] and to enhance the thermoelectric performance[11] of nanoelectronic devices with organic functional units.

Recently, experimental evidence of destructive QI was clearly observed in molecular junctions involving benzene,[12] terphenyl,[13] anthanthrene[14], antraquinone,[15], fullerenes and porphyrins,[16] as well as several other molecules with an organic backbone.[17] Sharp resonances in the differential conductance, the fingerprint of destructive QI, has been clearly detected even at room temperature.[18,19] In some cases, the agreement between experiments and density functional theory calculations,[14,17,20] as well as with predictions made by graphical rules,[20] is remarkable, thus establishing a scenario in which QI antiresonances can be regarded as robust features of quantum junctions, thus paving the way towards the realization of atomic-scale engineered quantum coherent devices.

Poly-phenyl molecular systems, or, more generally, alternant hydrocarbons with delocalized π orbitals represent the natural platform for QI effects. Remarkably, graphene nanostructures also fall into this category. Indeed, recent experiments reported QI patterns in graphene nanoconstrictions,[21] or bridges,[22] and break junctions,[18,19,23] What is more important, quantum junctions with graphene functional blocks benefit from all the extraordinary properties of graphene. Their chiral nature enables the manipulation of spin[24] and valley[25–29] degrees of freedom, while appropriate engineering of the substrate and gating offer the possibility to realize superlattices[30] and to tune the properties of the junction. Furthermore, the presence of edges and reduced dimensionality offer the possibility to enhance correlation effects and to induce magnetic order, absent in pristine graphene,[24,31–33] thus paving the way to a wide range of applications. Very recently, for instance, edge magnetism was stabilized in graphene nanoribbons functionalized with stable magnetic radical groups, demonstrating spin coherence times in the range of microseconds at room temperature.[24]

The present work is related to all these aspects. By means of numerical calculations and a detailed symmetry analysis, we show that QI effects can be used to control spin and valley polarization of ballistic transport in graphene quantum junctions up to room temperature in the absence of external magnetic fields. In particular, we show that both spin filtering and valley filtering can be achieved in the same device by simply tuning the coupling with a substrate to switch the nature of the site-site correlations in the functional element between ionic and antiferromagnetic.

The paper is organized as follows. In Sec. II we discuss the model and the methods used to tackle the problem of correlated transport and QI effects in graphene nanostructures. In Sec. III we discuss the interplay between destructive QI and different kinds of symmetry-breaking, and we provide a unified description of the phenomenon. In Sec. IV we explore the occurrence of the QI anti-resonances from a Green's function perspective, which allows us to pinpoint their origin. Finally, Sec. V contains our conclusions and an outlook.

II. GRAPHENE QUANTUM JUNCTIONS

We consider the quantum junction schematically depicted in Fig. 1. The Hamiltonian of the junction ($\mathcal{H}$) can be decomposed in three terms, which describe the nanoflake ($\mathcal{H}_F$), the leads ($\mathcal{H}_L$), and the tunneling between the leads and the flake ($\mathcal{H}_T$), respectively

$$\mathcal{H} = \mathcal{H}_F + \mathcal{H}_T + \mathcal{H}_L. \tag{1}$$

The relevant features of the nanoflake are captured by the following low-energy effective Hubbard model for the delocalized π electrons

$$\begin{aligned}\mathcal{H}_F = &-t\sum_{\langle ij\rangle\sigma} p^\dagger_{i\sigma}p_{j\sigma} - \mu\sum_{i\sigma} n_{i\sigma} + U\sum_i n_{i\uparrow}n_{i\downarrow} \\ &+\epsilon\sum_\sigma\Big(\sum_{i\in A} n_{i\sigma} - \sum_{i\in B} n_{i\sigma}\Big).\end{aligned} \tag{2}$$

where $p^\dagger_{i\sigma}$ ($p_{i\sigma}$) create (annihilate) an electron at lattice site i with spin σ, and $n_{i\sigma} = p^\dagger_{i\sigma}p_{i\sigma}$ is the electron density operator. The parameter t denotes the nearest-neighbor hopping amplitude on the honeycomb lattice, μ is the chemical potential, and the Hubbard U describes the onsite Coulomb repulsion. Here, ϵ is an onsite energy that explicitly breaks the chiral symmetry between the A and B graphene sublattices, which can be induced, e.g., by the interaction between graphene and a suitable substrate, such as hexagonal boron-nitride (h-BN).

The metallic electrodes and the tunneling Hamiltonians, $\mathcal{H}_L$ and $\mathcal{H}_T$, are instead given by

$$\begin{aligned}\mathcal{H}_L &= \sum_{\alpha k\sigma}\epsilon_{\alpha k\sigma}c^\dagger_{\alpha k\sigma}c_{\alpha k\sigma}, \\ \mathcal{H}_T &= \sum_{\alpha ik\sigma}\Big(V_{\alpha ik\sigma}c^\dagger_{\alpha k\sigma}p_{i\sigma} + V^*_{\alpha ik\sigma}p^\dagger_{i\sigma}c_{\alpha k\sigma}\Big),\end{aligned} \tag{3}$$

where the operators $c^\dagger_{\alpha k\sigma}$ ($c_{\alpha k\sigma}$) create (annihilate) an electron with energy $\epsilon_{\alpha k\sigma}$ in lead α, and $V_{\alpha ik\sigma}$ denotes the hopping amplitude between lattice site i of the nanoflake and state k of lead α. We consider a hexagonal zig-zag edge graphene nanoflake with $N = 54$ C atoms and a C_3 rotation symmetry around the center. As discussed in Ref. 5, destructive QI effects arise in contact configurations analogous to the *meta* configuration of a benzene molecular junction. In the meta configuration for the nanoflake, the leads are connected at edge sites that belong to the same graphene sublattice. As depicted in Fig. 1, there are two possibilities to realize such a configuration, i.e., when the edges belong to either the A or the B sublattice.

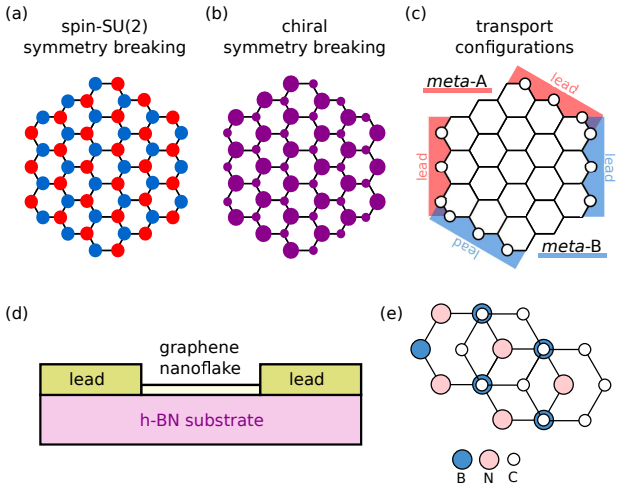

FIG. 1. (Color online) Schematic representations of (a) AF order in spin-SU(2) symmetry-broken case, where red (blue) circles represent spin-↑ (spin-↓) ordered magnetic moments, and (b) charge order in the chiral symmetry-broken case, where the size of the circle is proportional to the local charge density. (c) Two possible realizations of *meta* contact configurations, i.e., at edge atoms from either sublattice A or sublattice B. (d) Quantum junction with a functional block consisting of a hexagonal graphene nanoflake with zigzag edges, which is deposited on a h-BN substrate and is connected to two metallic leads. (e) Equilibrium stacking of the graphene/h-BN bilayer.

The Green's function of the nanoflake in the presence of the leads is obtained by solving the Dyson equation

$$G^{-1}_{ij}(\omega) = G^{-1}_{0,ij}(\omega) - \Sigma^L_{ij}(\omega) - \Sigma^R_{ij}(\omega) - \Sigma_{ij}(\omega), \tag{4}$$

where $G^{-1}_{0,ij}(\omega)$ is the bare Green's function of the isolated nanoflake, which is renormalized by three self-energy contributions: $\Sigma^L_{ij}(\omega)$ and $\Sigma^R_{ij}(\omega)$, which describe the embedding of the nanoflake with the left (L) and right (R) lead, respectively, and $\Sigma_{ij}(\omega)$, which describe the electronic correlations stemming from the Hubbard interaction U within the nanoflake.

The leads contribution to the self-energy is given by

$$\Sigma^\alpha_{ij\sigma}(\omega) = \sum_k \frac{V_{\alpha ik\sigma}V^*_{\alpha jk\sigma}}{\omega + \imath\eta - \epsilon_{\alpha k\sigma}}, \tag{5}$$

where $\eta > 0$ regularizes the analytic continuation. The product $V_{\alpha ik}V^*_{\alpha jk}$ in Eq. (5) describes virtual hopping processes in which an electron from site i of the nanoflake is injected into state k of lead α and (after a certain time) returns to site j of the nanoflake. In the following, we restrict to *local* hybridization processes, i.e., $\Sigma^\alpha_{ij} \propto \delta_{ij}$, without affecting the qualitative results presented below. Moreover, since the QI properties originate from

the topology of the nanoflake, and are independent of the details of the coupling with the leads, it is reasonable to assume a wideband limit (WBL) approximation for the leads,[34] in which $\Sigma^{\alpha}_{ii} = -\imath\Gamma$ and it is independent of energy for each contact site i.

The effects of electronic correlations within the nanoflake are taken into account within the dynamical mean-field theory[35] (DMFT), in a real-space extension suitable to deal with systems where the translational symmetry is broken in one or more spatial dimensions.[36–41] This approach is also suitable to treat inhomogeneous systems in the presence of charge-[42,43] and spin-order,[5,36,44,45] which will be of importance in the following, as well as superconductivity.[46] Within real-space DMFT, the nanoflake is mapped onto a set of self-consistent auxiliary Anderson impurity problems, which are solved with a Lánczos exact diagonalization procedure,[47,48] yielding a *local* yet site-dependent self-energy $\Sigma_{ij}(\omega) = \Sigma_i(\omega)\delta_{ij}$. Within this approximation, local quantum fluctuation are treated non-perturbatively, whereas non-local spatial correlations are retained at a static mean-field level.

At the same time, DMFT also allows us to take into account finite temperature effects within the Green's function formalism. This includes the broadening of the Fermi-Dirac distribution function as well as non-trivial effects of the temperature evolution of the many-body states. In the following, we consider temperature effects at $T = 0.005t$, which corresponds to $T \approx 150$ K for a realistic value of $t = 2.7$ eV of the nearest-neighbor hopping in graphene.[49]

Starting from the Green's function of the nanoflake, under appropriate assumptions,[50–52] the transmission of the junction can be estimated with the following Landauer-Büttiker expression[53,54]

$$T(\omega) = \mathrm{Tr}\Big[\Gamma^{L} G^{a} \Gamma^{R} G^{r}\Big], \tag{6}$$

where $G^{r(a)}$ is the retarded (advanced) Green's function obtained from Eq. (4), while the matrix $\Gamma^{\alpha} = \imath\big[\Sigma^{\alpha} - \Sigma^{\dagger\alpha}\big]$ encloses the spectral information of the leads. Within our description of the leads, the transmission in Eq. (6) can be recast as

$$T(\omega) = \sum_{\ell} \sum_{r} \Gamma^{L}_{\ell\ell}\, \Gamma^{R}_{rr} |G^{r}_{\ell r}(\omega)|^2, \tag{7}$$

which represents a sum over *independent* transmission channels, with ℓ and r labeling the lattice sites of the nanoflake connected to the L and R leads, respectively.

As is evident from Eq. (7), the energy dependence of the transmission is controlled entirely by the Green's function, thus establishing a direct relation between the transport properties of the junction and the electronic properties of the graphene nanoflake. It can be explicitly shown that corrections to the transmission function beyond the WBL do not change qualitatively the results presented in the following.[55]

This is particularly relevant because it is possible to link the existence of destructive QI to the symmetries and the analytic properties of the Green's function (see Sec. IV and Appendix A). This suggests that the extraordinary filtering properties of the device in the spin- and valley- channels are robust features, which depend neither on the details of the nanoflake and of the lead-flake hybridization, nor on the approximation employed in the calculations.[5]

III. RESULTS AND DISCUSSION

In the following we discuss the electronic and transport properties of the hexagonal graphene nanoflake quantum junction. In particular, we focus on the interplay between the destructive QI in the meta configuration and the symmetry breaking phenomena involving the spin- and valley- degrees of freedom.

A. Effects of the symmetry breaking on a destructive QI antiresonance

To realize the scenario in which we are interested, the minimal requirements for the transmission function $T_{\lambda}(\omega)$ are as follows: (i) $T_{\lambda}(\omega)$ displays a QI antiresonance at $\omega = \omega^{QI}_{\lambda}$ in a given channel, denoted by λ, which has two (or more) components; (ii) $T_{\lambda}(\omega)$ is the same for each component of λ, at least close to ω^{QI}_{λ}, when the symmetry associated with λ is not broken.

In the present case, the previous requirements are fulfilled, in any of the meta contact configurations of the junction, for both the spin and valley pseudo-spin (i.e., $\lambda = \{\sigma, \tau\}$, with $\sigma = \pm 1$ and $\tau = \pm 1$). When the $SU(4)$ symmetry associated with the combined degrees of freedom is intact, we observe a QI antiresonance with multiplicity $g_{\lambda} = 4$, while breaking the spin- or the chiral-$SU(2)$ symmetry (or both) results in a lifting of the degeneracy of ω^{QI}_{λ} and a strong differentiation of the transport properties due to the destructive QI. We summarize our findings in Fig. 2, where we show how the transmission $T(\omega)$ changes when breaking the symmetries of the Hamiltonian. When neither the spin nor the valley degeneracy is lifted, $T(\omega)$ is the same in all channels and displays a four-fold antiresonance at $\omega^{QI} = 0$, signature of destructive QI. This scenario is depicted in Fig. 2(b), while Fig. 2(a, c, and d) correspond to all the different symmetry-breaking scenarios, which we are going to discuss below in details.

B. Spin-split scenario

The ground state of the nanoflake changes from paramagnetic (PM) to antiferromagnetic (AF) when the local repulsion overcomes a critical threshold ($U > U^{AF}$). The AF state breaks the spin-$SU(2)$ symmetry, with a Néel-like pattern of ordered moments $\langle S^{z}_{i}\rangle = \langle n_{i\uparrow}\rangle - \langle n_{i\downarrow}\rangle$, which

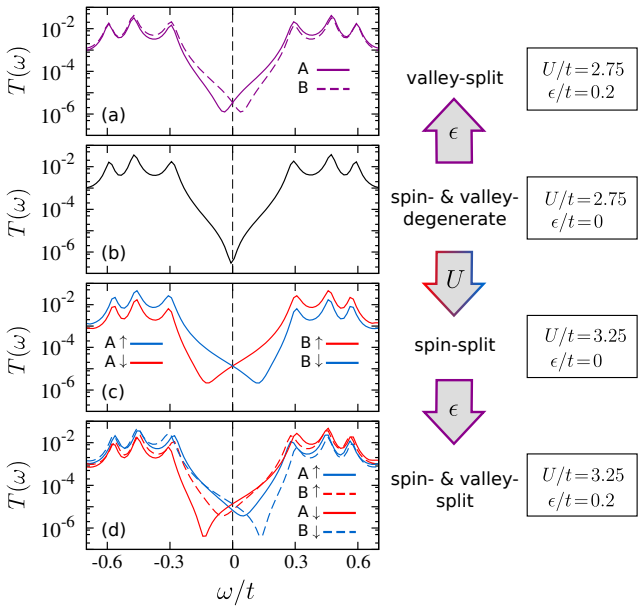

FIG. 2. (Color online) Evolution of $T_\lambda(\omega)$ in the spin- and valley- transmission channels. By breaking the spin-$SU(2)$ or the chiral symmetry (or both) the four-fold degeneracy ($g_\lambda = 4$) of the QI antiresonance at $\omega^{QI} = 0$ is lifted, and $g_\lambda = 2$ or $g_\lambda = 1$ QI antiresonances at $\omega_\lambda^{QI} \neq 0$ appear in the corresponding channel. The curves of each case are shifted vertically for clarity. Parameters: $\Gamma/t = 0.02$, $T/t = 0.005$, while U/t and ϵ/t as labeled.

have opposite polarization in the two graphene sublattices, and a finite staggered magnetization

$$\langle S^z\rangle = \frac{1}{N}\Big(\sum_{i\in A}\langle S_i^z\rangle - \sum_{i\in B}\langle S_i^z\rangle\Big). \tag{8}$$

The local magnetic moments are spatially inhomogeneous, and they increase with the distance from the center of the nanoflake.[44,56,57] The magnetic pattern is stabilized by short-range antiferromagnetic correlations, which are stronger at the edges and weaker in the bulk.[44] In the spin-$SU(2)$ symmetry-broken state, the transmission for a given valley is no longer the same in the spin-↑ and spin-↓ channels. The spin-resolved transmission $T_\sigma(\omega)$ still exhibits destructive QI, but the antiresonances are separated in energy and located at $\omega_\sigma^{QI} \propto \sigma\langle S^z\rangle$, as shown in Fig. 2(c) and in Fig. 3 explicitly.

The selective suppression of the transmission in one of the spin channels, due to destructive QI, can be exploited to obtain a *nearly perfect* QI-assisted spin-filtering device, as recently proposed in Ref. 5, which demonstrates the potential impact of the investigated phenomenon for technological applications. Note that, since the two sublattices have opposite magnetization, the transmission is still symmetric under the simultaneous inversion of the spin ($\sigma \to \bar\sigma$) and valley pseudospin ($\tau \to \bar\tau$) i.e., $T_{\tau\sigma}(\omega) = T_{\bar\tau\bar\sigma}(\omega)$, as specified in the legend of Fig, 2. This means also that the QI antiresonance is still two-fold degenerate $\omega_{\tau\sigma}^{QI} = \omega_{\bar\tau\bar\sigma}^{QI}$.

The transport properties of the junction in this scenario are shown in details in Fig. 3. The top panels show the heatmap of $T_\sigma(\omega)$ as a function of ω/t and U/t separately for the spin-↑ and spin-↓ channels (for valley B, but the situation is analogous for valley A, as discussed above). From the point of view of the electronic structure, the information enclosed in the transmission function is equivalent to that of the electronic excitation spectrum. Indeed, one can follow the evolution of the electronic resonances (darker shades of color in the heatmap) and in particular, of the ones closest to the Fermi level, corresponding to the ighest occupied molecular orbital and the lowest unoccupied molecular orbital, which identify the spectral gap. At $U/t < U^{AF}/t \lesssim 3$, the gap is *reduced* with respect to its non-interacting value[44] as $\Delta \approx \langle Z\rangle\Delta_0$, where $\langle Z\rangle$ is the average over the nanoflake of local quasi-particle residue, extracted from the local DMFT self-energy as

$$Z_i = \Big(1 - \frac{\partial\Sigma_i(\omega)}{\partial\omega}\Big|_{\omega\to 0}\Big)^{-1}. \tag{9}$$

Instead, when AF sets in, the gap is no longer controlled by the quantum confinement effect, but by the staggered magnetization, and it *increases* with U. While the transmission is exponentially suppressed within the energy gap, destructive QI manifests itself in the form of a QI antiresonance (in the middle of the white area in the heatmap). In the PM state, the anti-resonance is *pinned* at the Fermi level $\omega^{QI} = 0$ due to the particle-hole symmetry of the spectrum.[5,58] In the AF state instead ω_σ^{QI} is spin-dependent and shifts below or above the Fermi level, proportionally to the average staggered magnetization $\langle S^z\rangle$. The detailed analysis of the transmission as a function of U/t shown in Fig. 3 explains the change in the transmission Figs. 2(b,c) in between the symmetric and the spin-split scenarios.

As a consequence of the different behavior of $T_\uparrow(\omega)$ and $T_\downarrow(\omega)$, the spin-polarization of the transmission

$$\zeta_\sigma(\omega) = \frac{T_\uparrow - T_\downarrow}{T_\uparrow + T_\downarrow}, \tag{10}$$

is not zero in a wide frequency range above and below the Fermi level. This is demonstrated in the bottom panels of Fig. 3, where we show the heatmap of $\zeta_\sigma(\omega)$ as a function of ω/t and U/t, as well as cuts of $\zeta_\sigma(\omega)$ for specific values of U/t. In all cases, the maxima (or minima) of the polarization located at frequencies ω_σ^{QI}, where the transmission probability in one spin channel is strongly suppressed and the transport is dominated by the other channel, thus achieving *nearly perfect* spin filtering.[5]

C. Valley-split scenario

Let us consider the case in which $U < U^{AF}$ and the ground state of the system is therefore PM, and let us introduce a field that breaks the chiral symmetry, associated with the chemical equivalence of the graphene

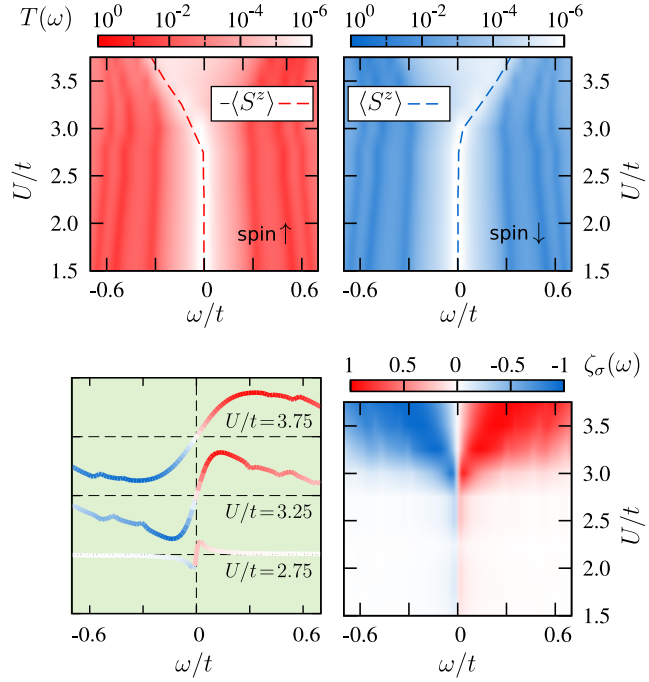

FIG. 3. (Color online) Interplay between destructive QI and spin-$SU(2)$ symmetry breaking. Map of the spin-resolved transmission $T_\sigma(\omega)$ (top panels). The dashed lines show the relation $\omega_\sigma^{QI}\approx\sigma\langle S^z\rangle$, while the gap can be estimated by the energy difference of the lowest-energy (HOMO and LUMO) transmission resonances. Map of the spin polarization $\zeta_\sigma(\omega)$ and corresponding cuts at different values of U/t (lower panels). Parameters: $\epsilon/t=0$, $\Gamma/t=0.02$, and $T/t=0.005$. The data shown are for valley B, but the results are analogous for valley A, when the proper symmetry relations are considered, as discussed in the text.

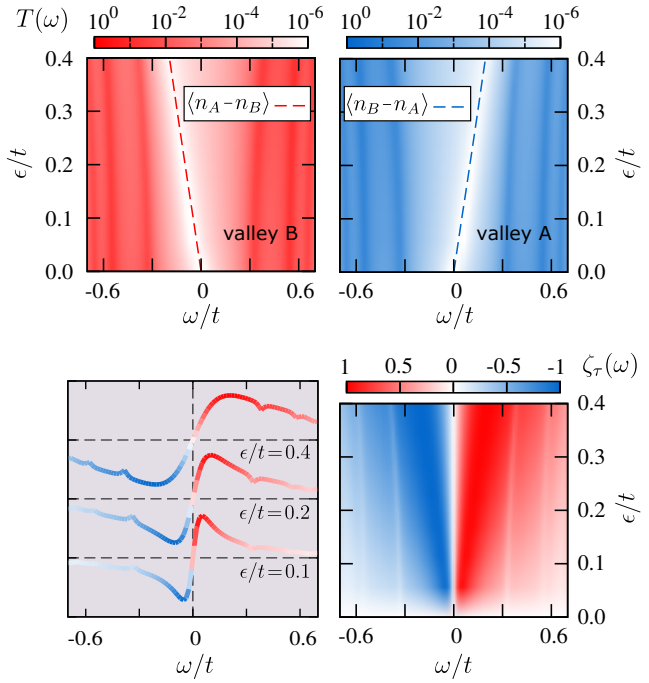

FIG. 4. (Color online) Interplay between destructive QI and chiral symmetry breaking. Map of the valley-resolved transmission $T_\tau(\omega)$ (top panels). The dashed lines show the relation $\omega_\tau^{QI}\approx\tau\langle n_A-n_B\rangle$, while the gap can be estimated by the energy difference of the lowest-energy (HOMO and LUMO) transmission resonances. Map of the pseudo-spin polarization $\zeta_\tau(\omega)$ and corresponding cuts at different values of ϵ/t (lower panels). Parameters: $U/t=1.5$, $\Gamma/t=0.02$, and $T/t=0.005$. The data shown are for the spin-↑ channel, but the result are identical for the spin-↓ channel, due to the spin-$SU(2)$ symmetry, as discussed in the text.

sublattices. Here we assume that this term originates from the interaction between graphene and a h-BN substrate. Indeed, *ab-initio* density functional theory calculations have shown that in graphene/h-BN bilayers, in the equilibrium stacking position, the atoms of one of the two graphene sublattices iare stacked on top of B atoms, while the atoms of the other sublattice are located in the hollow position of the underlying h-BN honeycomb lattice.[59] Following Skomski *et al.*,[60] the asymmetric adsorption of the graphene sublattices can be encoded in a single-particle term ϵ, which has the form given in Eq. (2) in the Hamiltonian of the nanoflake.

The chiral symmetry-breaking field ϵ induces a charge-density wave (CDW) and drives the C atoms *locally* away from half-filling (while the electric charge is overall conserved). At $\epsilon\neq0$ the two valleys are no longer degenerate and each of the valley-resolved transmission functions $T_\tau(\omega)$, shown in Fig. 2(a), displays a destructive QI antiresonance at $\omega_\tau^{QI}\approx\tau\langle n_A-n_B\rangle$, where

$$\langle n_{A/B}\rangle=\frac{2}{N}\sum_\sigma\sum_{i\in A/B}\langle n_{i\sigma}\rangle \tag{11}$$

is the sublattice-resolved charge density. Note that, analogously to the previous case, $T_\tau(\omega)$ retains a two-fold degeneracy due to the spin-$SU(2)$ invariance, and therefore $\omega_{\tau\sigma}^{QI}=\omega_{\tau\bar\sigma}^{QI}$.

The analysis of the transport properties is presented in Fig. 4 and can be done in complete analogy with that of the spin-split scenario. For this reason, we mostly focus on the differences between the two cases. The heatmap of $T_\tau(\omega)$ as a function of ω/t and ϵ/t shows that the spectral gap *increases* for any $\epsilon>0$, and ω_τ^{QI} shifts away from the Fermi level proportionally to the charge-density wave order parameter. In contrast to the previous case, there is no finite critical threshold for the onset of the charge-density wave. The valley-polarization of the transmission $\zeta_\tau(\omega)$, defined as

$$\zeta_\tau(\omega)=\frac{T_A-T_B}{T_A+T_B} \tag{12}$$

is finite for any $\epsilon\neq0$. The maxima (or minima) of the polarization $\zeta_\tau(\omega)$ are always located at frequencies ω_τ^{QI}, where the transmission probability in one valley channel is strongly suppressed and the transport is therefore dominated by the other channel. This corresponds to a *nearly perfect* valley filtering.

D. Spin- and valley-split scenario

Lastly, we consider the case in which both the spin- and the chiral-$SU(2)$ symmetries are broken. It is more intuitive to take the spin-split scenario above as a starting point and break the chiral symmetry with the ϵ field. As shown in Fig. 2(d), the QI antiresonance of each valley splits under the effect of ϵ, further reducing the degeneracy of ω_λ^{QI} to $g_\lambda = 1$. It is obvious that a completely equivalent description is obtained by taking the valley-split scenario as a starting point and increasing U above U^{AF} to induce magnetic order. Let us note that there is a non-trivial feedback between charge- and spin- correlations, resulting in a (weak) dependence of the critical threshold for spin ordering on the chiral symmetry-breaking field, i.e., $U^{AF} = U^{AF}(\epsilon)$. In fact, the formation of a charge-density wave requires to locally drive the C atoms away from half-filling. This is detrimental to the formation of the AF state, and it results in a partial quench of the local magnetic moments.[5] A consequence of this interplay is that, if the system is on the verge of magnetic ordering, tuning ϵ could allow to drive the system through a crossover between phases with different charge and spin order, and ideally working as a switch between spin-filtering and valley-filtering effects.

Due to the finiteness of the system, it is not trivial to obtain a reliable estimate of $U_{AF}(\epsilon)$. There is however an alternative way to visualize this effect. In Fig. 5(a) we show the magnetic order parameter $\langle S_z \rangle$, which is suppressed by ϵ at any value of U. However, we note that it is difficult to reduce the order parameter below a certain numerical threshold since the observables for two spin components are evaluated independently. At the same time, the CDW order parameter $\langle n_A - n_B \rangle$ increases linearly with ϵ. In Fig. 5(b) we show a phase diagram, characterized by the quantity

$$\phi = \frac{|\langle S_z \rangle| - |\langle n_A - n_B \rangle|}{|\langle S_z \rangle| + |\langle n_A - n_B \rangle|}, \tag{13}$$

which measures the relative weight of the AF and CDW order parameters. Hence, as $\phi(U, \epsilon) \to -1$, it highlights a crossover towards a pure CDW state (i.e., without AF order) and provides a reasonable estimate of $U_{AF}(\epsilon)/t$, as indicated by the dashed line (guide to the eye).

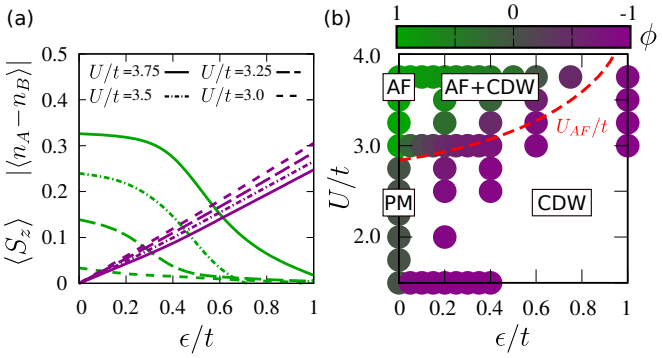

FIG. 5. (a) Evolution of the magnetic order parameters $\langle S_z \rangle$ (green lines) and the CDW order parameter $|\langle n_A - n_B \rangle|$ (violet lines) with ϵ/t for different values of U/t. (b) Phase diagram identifying the PM and the AF (at $\epsilon = 0$) as well as the CDW and the AF+CDW states. The quantity ϕ (see definition in the text) measures the weight of the different order parameters. The red dashed line separating the AF+CDW and the CDW states is to be intended as a guide to the eye indicating the crossover between the two states rather than a true estimate of $U_{AF}(\epsilon)$.

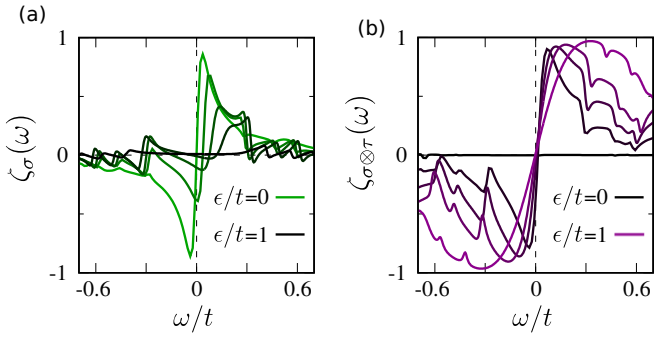

FIG. 6. Evolution with ϵ/t at $U/t = 3$ of the spin-filtering efficiency $\zeta_\sigma(\omega)$ (for valley B, while the results for valley A can be obtained by symmetry) an the generalized valley-filtering efficiency $\zeta_{\sigma\otimes\tau}(\omega)$. Upon increasing the strength of the chiral symmetry-breaking field from $\epsilon/t = 0$ to $\epsilon/t = 1$ (in steps of $\Delta\epsilon = 0.2$) $\zeta_\sigma(\omega)$ is suppressed (green to dark shades) while $\zeta_{\sigma\otimes\tau}(\omega)$ is enhanced (dark to violet shades) thus driving the system from a pure spin filter towards a pure valley filter.

At the same time, the crossover from a spin filter to a valley filter can be observed directly by looking at the polarization of the transmission function across the $U_{AF}(\epsilon)$ line in parameter space. It is very intuitive to look at it as a function of ϵ/t at a fixed value of U/t, as shown in Figs. 6(a-b) for $U/t = 3$. In Fig. 6(a) we show the spin-filtering efficiency $\zeta_\sigma(\omega)$. At $\epsilon = 0$ it displays two strong peaks at $\omega = \omega_\sigma^{QI}$, which identify the destructive QI antiresonances causing the transport to be dominated by one spin channel. As ϵ/t increases both peaks are shifted to higher energy due to the inversion-symmetry breaking and are progressively suppressed as the AF order parameter $\langle S^z \rangle$ is suppressed, until the spin-filtering efficiency substantially vanishes. In order to quantify the valley filtering efficiency in the regime where both the spin-SU(2) and the valley-SU(2) symmetries are lifted, it is convenient to consider the quantity

$$\zeta_{\sigma\otimes\tau} = \frac{T_{A\uparrow} - T_{B\downarrow}}{T_{A\uparrow} + T_{B\downarrow}}, \tag{14}$$

which properly takes into account the fact that in the presence of AF order opposite valleys have also opposite spin polarization. In particular, $\zeta_{\sigma\otimes\tau}(\omega) \equiv 0$ if $\epsilon/t = 0$ even if $\langle S_z \rangle \neq 0$, which is not true in the case of the quantity $\zeta_\tau(\omega)$ as defined in Eq. (12). In Fig. 6(b) we show that is strongly enhanced over an increasingly wider energy window as ϵ/t increases.

Combining these two pieces of information demonstrates that, eventually, the chiral symmetry-breaking drives the system from a pure spin filter into a pure valley-filter.

IV. ORIGIN OF THE QI ANTIRESONANCES

To understand the mechanism leading to the ω^{QI} degeneracy lifting, we look explicitly at the structure of the Green's function.

As already discussed, the general Landauer expression for the transmission function can be recast as in Eq. (7), which establishes a direct link between $T(\omega)$ and $G_{\ell r}(\omega)$ for the generic $\ell \to r$ channel. In particular, in the WBL, all the frequency dependence of $T(\omega)$ comes from the Green's function. This means that a QI antiresonance (i.e., a zero of the transmission) necessarily implies a zero of the Green's function. At energies $|\omega| < \Delta$ (i.e., within the spectral gap) $\Im G_{\ell r}(\omega) \approx 0$ for every pair (ℓ, r), where the exact relation holds at $T = 0$. Therefore the zeroes of the Green's function coincide with the zeros of $\Re G_{\ell r}(\omega)$. It can be shown (see Appendix A 1 for the derivation) that when neither the spin-$SU(2)$ nor the chiral symmetry is broken, the zero of the Green's function is pinned at the Fermi level ($\omega = 0$) by the particle-hole symmetry. Instead, any symmetry-breaking term shifts the zeros of $\Re G_{\ell r}(\omega)$, and hence the destructive QI antiresonance at finite frequency (see Appendix A 2).

In order to demonstrate this effect, in Fig. 7 we explicitly show the low-energy structure of $\Re G_{\ell r}(\omega)$, for a given transmission channel, in which ℓ and r are the sites in the middle of the L and R edges in the meta configuration (of sublattice B). The case of sublattice A can be obtained from this one by symmetry. In the upper panel of Fig. 7 we show the effect of the spin-$SU(2)$ symmetry breaking. In the PM state, the zero of $\Re G_{\ell r}(\omega)$ is found at $\omega = 0$ for both the spin-$\uparrow$ and spin-$\downarrow$ channels, while in the AF state we observe an opposite shift of the zeros to finite frequency which correlates with the behavior of the destructive QI antiresonance found at ω_σ^{QI}, as shown in Fig. 2(c) (for sublattice B). In the lower panel of Fig. 7 we demonstrate the analogous effect in for the chiral symmetry breaking. Contrary to the previous case, at $\epsilon = 0$, $\Re G_{\ell r}(\omega)$ is not identical for the two valleys, but both display a zero at $\omega = 0$. At finite field ϵ, the zeros split symmetrically with respect to the Fermi level, yielding different ω_τ^{QI} for the two valleys.

While an analytic expression for ω_λ^{QI} in the generic case cannot be easily obtained, in Appendix A we provide an argument that explains the relation between ω_λ^{QI} and the order parameters $\langle S^z \rangle$ and $\langle n_A - n_B \rangle$, which is shown in Figs. 3 and 4 for the two symmetry-broken states, respectively. In particular, we stress that the shift of the zeros of the Greens function is controlled by the low-frequency behavior of $\Re \Sigma_{ii}(\omega)$. This can be significantly different from the large-frequency one, which in turn can be seen as a sort of mean-field value. The difference between the low-frequency and high-frequency values of the self-energy can be taken as an estimate of the dynamical correlations beyond mean-field, and it has been shown to influence qualitatively the physics in models with a non-trivial band topology.[45,61]

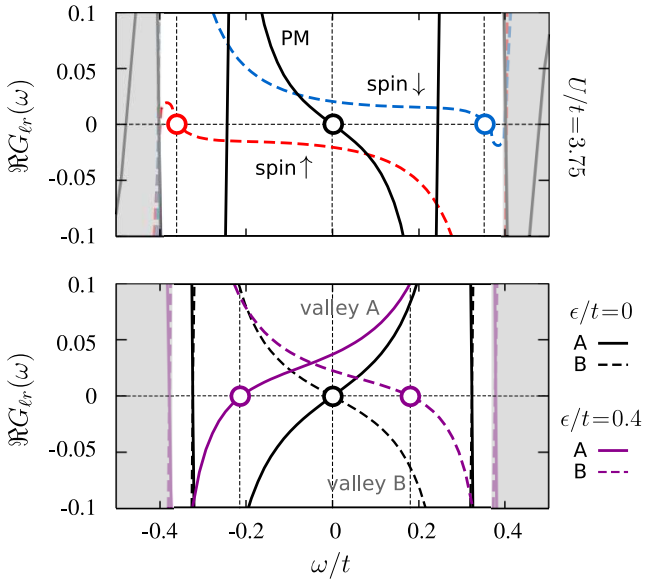

FIG. 7. (Color online) Zeros of the $\Re G_{\ell r}(\omega)$ for the sites in the middle of the edges of the meta configuration, without and with symmetry breaking. In the spin-split scenario for valley A (upper panel) and in the valley-split scenario for spin-$\uparrow$ (lower panel), the two-fold degeneracy of the zero at $\omega_0 = 0$ is lifted, yielding two zeros at $|\omega_0^\uparrow| = |\omega_0^\downarrow| \approx \langle S^z \rangle \approx 0.33$, and two zeros at $|\omega_0^A| = |\omega_0^B| \approx \langle n_B - n_A \rangle \approx 0.19$, respectively. The grey shaded area indicates the energy window lying *outside* the broken-symmetry gaps. Parameters: $U/t = 3.75$, $\epsilon/t = 0$, $\Gamma/t = 0.02$ and $T = 0.005t$ (upper panel); $U/t = 1.5$, $\epsilon/t = 0$ and $\epsilon/t = 0.4$, $\Gamma/t = 0.02$ and $T = 0.005t$ (lower panel).

V. CONCLUSIONS & OUTLOOK

We investigated the interplay between destructive QI and symmetry-breaking phenomena involving the spin and valley degrees of freedom in graphene nanoflakes. Specifically, by establishing a relation between the analytic structure of the real-space Green's function and the symmetries of the Hamiltonian, we provide a clear understanding of the origin of the QI antiresonances and of their effects on ballistic transport. Interestingly, our analysis works both in the symmetric and in the symmetry-broken cases, and we show that breaking a symmetry shifts the position of the antiresonance, without spoiling the destructive QI effects. This demonstrates the generality and the robustness of the phenomenon within a generic theoretical framework and also in the presence of electron-electron interactions. Ultimately, it allows us to predict the occurrence of QI antiresonances in complex nanostructures interacting with the environ-

ment.

In our original proposal in Ref. 5, we showed that destructive QI can be used to generate nearly completely spin-polarized currents in the absence of magnetic fields or spin-orbit coupling, simply exploiting the spontaneous breaking of the $SU(2)$ spin-rotational symmetry induced by electronic correlation in the presence of the edges. The present work extends the scope of our previous study to multi-component systems where other degrees of freedom (e.g., valley, orbital, layer) can be manipulated via an external handle lifting the symmetry. In the specific case considered here, the mechanisms involved are the onset of a magnetically ordered state (associated with the electron spin) and the breaking of the inversion symmetry due to the interaction with a specific substrate (associated with the valley). We show that a tuning the coupling between the nanoflake and the substrate can turn a spin filter into a valley filter.

The approach developed in the present work follows a general scheme according to which it is possible to manipulate the transport properties of a quantum junctions exploiting destructive QI, provided we have identified a symmetry and the corresponding symmetry-breaking control parameter. Other mechanisms suitable to this purpose are: (i) the switchable magnetic bistability of metal-organic complexes,[62] (ii) the Jahn-Teller distortions in charged fullerenes,[63] and (iii) the formation of a moiré pattern in twisted bilayer graphene junctions.[64]

In this respect, we believe that our work can drive the community towards a promising and -so far- only sporadically explored direction.

ACKNOWLEDGMENTS

We thank R. Stadler and C. Lambert for valuable discussions. We acknowledges financial support from MIUR PRIN 2015 (Prot. 2015C5SEJJ001) and SISSA/CNR project "Superconductivity, Ferroelectricity and Magnetism in bad metals" (Prot. 232/2015) and from the H2020 Framework Programme, under ERC Advanced Grant No. 692670 "FIRSTORM". V.B. acknowledges support from Regione Lazio (L.R. 13/08) through project SIMAP. A.V. acknowledges financial support from the Austrian Science Fund (FWF) through the Erwin Schrödinger fellowship J3890-N36.

Appendix A: Impact of symmetries on the real-space Green's function and the transmission

1. Symmetric state

At half-filling, the Hamiltonian of the flake $\mathcal{H}_F$ given in Eq. (2) is symmetric under the following particle-hole transformation

$$\begin{aligned} p^\dagger_{Ai\sigma} &\to p_{Ai\sigma} & \qquad p_{Ai\sigma} &\to p^\dagger_{Ai\sigma} \\ p^\dagger_{Bi\sigma} &\to -p_{Bi\sigma} & \qquad p_{Bi\sigma} &\to -p^\dagger_{Bi\sigma}. \end{aligned} \tag{A1}$$

The pinning of the destructive QI antiresonance at the Fermi level can be demonstrated by considering the definition of the retarded Green's function

$$G^r_{ij\sigma}(\omega) = -i \int \theta(t) \left\langle \left\{ p_{i\sigma}(t), p^\dagger_{j\sigma}(0) \right\} \right\rangle e^{-i\omega t} \mathrm{d}t, \tag{A2}$$

where $\theta(t)$ is the Heaviside function, $\{\cdot,\cdot\}$ is the anticommutator for the fermionic operators, and the average is taken over the ground state at $T = 0$, while it is replaced by the usual thermal average at $T \neq 0$. The invariance of the above expression under particle-hole transformation implies

$$G^r_{ij\sigma}(\omega) = -i(-1)^{i+j} \int \theta(t) \left\langle \left\{ p^\dagger_{i\sigma}(t), p_{j\sigma}(0) \right\} \right\rangle e^{-i\omega t} \mathrm{d}t \tag{A3}$$

where the prefactor $(-1)^{i+j}$ equals ± 1 depending on whether i and j belong to the same or to different sublattices. On the other hand, taking the complex conjugate of Eq. (A2) one obtains

$$\left[G^r_{ij\sigma}(\omega)\right]^* = i \int \theta(t) \left\langle \left\{ p^\dagger_{i\sigma}(t), p_{j\sigma}(0) \right\} \right\rangle e^{i\omega t} \mathrm{d}t. \tag{A4}$$

A comparison of equations Eq. (A3) and Eq. (A4) demonstrates that in the presence of particle-hole symmetry the following relation holds

$$\left[G^r_{ij\sigma}(\omega)\right]^* = (-1)^{i+j+1} G^r_{ij\sigma}(-\omega). \tag{A5}$$

This implies that, in the meta configuration, $\Re G_{ij\sigma}(0)$ is vanishing due to the particle-hole symmetry. Since $\Im G_{ij\sigma}(0)$ is suppressed by the presence of the spectral gap, the transmission from Eq. (7) becomes

$$T^{\mathrm{meta}}_\sigma(0) = \sum_{\ell r} \Gamma_{\ell\ell} \Gamma_{rr} |\Im G^r_{\ell r\sigma}(0)|^2 \approx 0, \tag{A6}$$

where ℓ and r span the proper subsets for the meta configuration. This demonstrates the pinning of the destructive QI at the Fermi level in the particle-hole symmetric case. Moreover, this implies that a destructive QI is expected for any transmission channel $\ell \to r$ connecting sites from the same sublattice,[5,58] which allows us to *predict* the occurrence of antiresonances in complex graphene nanostructures.

It is interesting to notice that the situation is drastically different in the other possible transport configurations. In both the ortho and para configurations, the sites i and j belong to different sublattices. Hence, Eq. (A5) implies that $\Im G_{ij\sigma}(0)$ is vanishing, while $\Re G_{ij\sigma}(0)$ is not. As a consequence, both $T^{\mathrm{ortho}}_\sigma(0)$ and $T^{\mathrm{para}}_\sigma(0)$ do not display any destructive QI antiresonance at the Fermi level.

Let us note that, in principle, an asymmetric coupling between the leads and the flake explicitly breaks the

particle-hole symmetry. However, in the WBL approximation, the leads introduce an additional lifetime $\Gamma_{\ell\ell}$ and Γ_{rr}, but they do not induce any energy shift to the poles, so that the excitation spectrum remains particle-hole symmetric. Furthermore, even in the case when the particle-hole is broken, the QI antiresonance would still exist at a finite frequency ω_λ^{QI}.

2. Symmetry-broken state

In the presence of AF short-range order with a Néel pattern, the particle-hole transformation Eq. (A1) has to be modified as follows, to leave the ground-state invariant

$$\begin{aligned} p^\dagger_{Ai\sigma} &\to p_{Ai\bar\sigma} & p_{Ai\sigma} &\to p^\dagger_{Ai\bar\sigma} \\ p^\dagger_{Bi\sigma} &\to -p_{Bi\bar\sigma} & p_{Bi\sigma} &\to -p^\dagger_{Bi\bar\sigma} \end{aligned} \tag{A7}$$

where $\bar\sigma = -\sigma$. In this case, Eq. (A5) becomes

$$\left[G^r_{ij\sigma}(\omega)\right]^* = (-1)^{i+j+1} G^r_{ij\bar\sigma}(-\omega), \tag{A8}$$

which yields the following relation for the spin-dependent conductance

$$T_\sigma(\omega) = T_{\bar\sigma}(-\omega) \tag{A9}$$

in all transport configurations (i.e., including also contact configurations of the nanoflake that do not exhibit destructive QI, such as the analogs of *ortho* and *para* configurations of benzene).

Since the AF order and the graphene sublattices share the same real-space pattern, we can equivalently define the particle-hole transformation as

$$\begin{aligned} p^\dagger_{Ai\sigma} &\to p_{Bi\sigma} & p_{Ai\sigma} &\to p^\dagger_{Bi\sigma} \\ p^\dagger_{Bi\sigma} &\to -p_{Ai\sigma} & p_{Bi\sigma} &\to -p^\dagger_{Ai\sigma} \end{aligned} \tag{A10}$$

where, with respect to Eq. (A7) we only exchanged the role of spin and sublattice indices.

Let us now analyze the consequences of the invariance of the Green's function under the particle-hole transformation in Eq. (A10). When the Green's function connects sites belonging to different sublattices, as in the ortho and para configurations, the invariance under Eq. (A10) implies

$$G^r_{ij}(\omega) = i \int \theta(t) \left\langle \left\{ p^\dagger_{j\sigma}(t), p_{i\sigma}(0) \right\} \right\rangle e^{-i\omega t} \mathrm{d}t \tag{A11}$$

that compared with Eq. (A4) yields

$$\left[G^{r,AB}_{ij\sigma}(\omega)\right]^* = -G^{r,AB}_{ji\sigma}(-\omega). \tag{A12}$$

where the superscript AB indicate that i and j belong to different sublattices. Eq. (A12) in turn implies for the total transmission in the ortho and para configurations $T_\sigma(\omega) = T_\sigma(-\omega)$, and along with Eq. (A9) eventually prevents the spin-filtering effect, yielding

$$T^{\mathrm{ortho}}_\sigma(\omega) = T^{\mathrm{ortho}}_{\bar\sigma}(\omega), \quad T^{\mathrm{para}}_\sigma(\omega) = T^{\mathrm{para}}_{\bar\sigma}(\omega). \tag{A13}$$

On the contrary, in the meta configuration, similar reasoning shows that invariance under Eq. (A10) implies

$$\left[G^{r,AA}_{ij\sigma}(\omega)\right]^* = G^{r,BB}_{ji\sigma}(-\omega) \tag{A14}$$

where the AA and BB superscripts indicate the two possible meta configurations, i.e., where only sites of sublattice A or only sites of sublattice B are connected to the leads.

Finally, Eq. (A14) implies the following relation for the transmission

$$T^{\mathrm{meta}}_{\sigma AA}(\omega) = T^{\mathrm{meta}}_{\sigma BB}(-\omega), \tag{A15}$$

that along with Eq. (A9) yields

$$T^{\mathrm{meta}}_{\sigma AA}(\omega) = T^{\mathrm{meta}}_{\bar\sigma BB}(\omega). \tag{A16}$$

Hence, provided that $\omega^{\mathrm{QI}}_\sigma \neq 0$, the above relations imply the spin- and sublattice- structure observed in the numerical simulations. Considering that in this case the AF and CDW order share the same real-space pattern, Eq. (A15) also demonstrates the properties of the chiral symmetry breaking case.

The last step of the analysis consists in the identification of the mechanism that shifts the QI antiresonance. Within DMFT, the spin-$SU(2)$ symmetry breaking is a spontaneous phenomenon. It is induced by the sort-range AF correlations due to the local repulsion U, resulting in a dynamical spin-dependent self-energy $\Sigma_\sigma(\omega)$. The static contribution of the self-energy $\Re\Sigma_\sigma(0) \propto \sigma\langle S^z\rangle$, acts as an effective chemical potential, with *opposite* sign for the two spin polarizations, and it shifts the zeros of the Green's function to $\omega^{\mathrm{QI}}_\sigma$. This effect is ultimately at the origin of the behavior observed in Fig. 7 (upper panel) for the spin-split case. The chiral symmetry is instead explicitly broken by the field, so that the effective correction to the zero of the Green's function is given by $\epsilon\tau + \Re\Sigma_\tau(0) \propto \langle n_A - n_B\rangle$. Both terms have *opposite* sign for the two valleys, and they induce the symmetric shift of the zeros to $\omega^{\mathrm{QI}}_\tau$, as observed in Fig. 7 (lower panel) for the valley-split case. Finally, in the spin- and valley-split case, the combination of the above self-energy corrections in the different channels can result in the complete lifting of the four-fold degeneracy of the QI antiresonance.

In general, the exact value of $\omega^{\mathrm{QI}}_\lambda$ in a given transmission channel depends on the details of the real-space magnetization and charge redistribution pattern. Moreover, the transmission through the junction is in general given by the sum over the contributions of different channels, as shown in Eq. (7). Hence, one might expect a distribution of antiresonances, one for each channel, which result in a broadening of the minima of the transmission with respect to the one pinned at the Fermi level and controlled by the particle-hole symmetry alone. Indeed, this effect is clearly observed in the numerical results.

[1] G. C. Solomon, D. Q. Andrews, T. Hansen, R. H. Goldsmith, M. R. Wasielewski, R. P. V. Duyne, and M. A. Ratner, J. Chem. Phys. **129**, 054701 (2008).
[2] D. M. Cardamone, C. A. Stafford, and S. Mazumdar, Nano Lett. **6**, 2422 (2006).
[3] C. A. Stafford, D. M. Cardamone, and S. Mazumdar, Nanotechnology **18**, 424014 (2007).
[4] D. Nozaki and C. Toher, J. Phys. Chem. C **121**, 11739 (2017).
[5] A. Valli, A. Amaricci, V. Brosco, and M. Capone, Nano Lett. **18**, 2158 (2018).
[6] M. Kagan, V. Val'kov, and S. Aksenov, Journal of Magnetism and Magnetic Materials **440**, 15 (2017).
[7] V. S. Protsenko and A. A. Katanin, Phys. Rev. B **99**, 165114 (2019).
[8] D. Li, R. Banerjee, S. Mondal, I. Maliyov, M. Romanova, Y. J. Dappe, and A. Smogunov, Phys. Rev. B **99**, 115403 (2019).
[9] D. Li, Y. J. Dappe, and A. Smogunov, arXiv **1906:01429** (2019).
[10] G. Calogero, I. Alcòn, N. Papior, A.-P. Jauho, and M. Brandbyge, J. Am. Chem. Soc. , Just Accepted (2019).
[11] M. Noori, H. Sadeghia, and C. J. Lambert, Nanoscale **9**, 5299 (2017).
[12] G. Yang, H. Wu, J. Wei, J. Zheng, Z. Chen, J. Liu, J. Shi, Y. Yang, and W. Hong, Chinese Chemical Letters **29**, 147 (2018).
[13] Y. Li, M. Buerkle, G. Li, A. Rostamian, H. Wang, Z. Wang, D. R. Bowler, T. Miyazaki, L. Xiang, Y. Asai, G. Zhou, and N. Tao, Nature Materials **18**, 357 (2019).
[14] Y. Geng, S. Sangtarash, C. Huang, H. Sadeghi, Y. Fu, W. Hong, T. Wandlowski, S. Decurtins, C. J. Lambert, and S.-X. Liu, J. Am. Chem. Soc. **137**, 4469 (2015).
[15] C. M. Guédon, H. Valkenier, T. Markussen, K. S. Thygesen, J. C. Hummelen, and S. J. van der Molen, Nature Nanotechnology **7**, 305 (2012).
[16] S. Gerlich, S. Eibenberger, M. Tomandl, S. Nimmrichter, K. Hornberger, P. J. Fagan, J. Tüxen, M. Mayor, and M. Arndt, Nat. Comm. **2**, 263 (2011).
[17] M. Gantenbein, L. Wang, A. A. Al-jobory, A. K. Ismael, C. J. Lambert, W. Hong, and M. R. Bryce, Scientific Reports **7**, 1794 (2017).
[18] A. Batra, J. S. Meisner, P. Darancet, Q. Chen, M. L. Steigerwald, C. Nuckolls, and L. Venkataraman, Faraday Discuss. **174**, 79 (2014).
[19] M. Famili, C. Jia, X. Liu, P. Wang, I. M. Grace, J. Guo, Y. Liu, Z. Feng, Y. Wang, Z. Zhao, S. Decurtins, R. Häner, Y. Huang, S.-X. Liu, C. J. Lambert, and X. Duan, Chem **5**, 474 (2019).
[20] T. Markussen, R. Stadler, and K. S. Thygesen, Nano Lett. **10**, 4260 (2010).
[21] P. Gehring, H. Sadeghi, S. Sangtarash, C. S. Lau, A. A. J. Liu, J. H. Warner, C. J. Lambert, G. A. D. Briggs, and J. A. Mol, Nano Lett. **16**, 4210 (2016).
[22] D. Nozaki, Lokamani, A. Santana-Bonilla, A. Dianat, R. Gutierrez, , and G. Cuniberti, J. Phys. Chem. Lett. **6**, 3950 (2015).
[23] S. Caneva, P. Gehring, V. M. García-Suárez, A. García-Fuente, D. Stefani, I. J. Olavarria-Contreras, J. Ferrer, C. Dekker, and H. S. J. van der Zant, Nature Nanotechnology **13**, 1126 (2018).
[24] M. Slota, A. Keerthi, W. K. Myers, E. Tretyakov, M. Baumgarten, A. Ardavan, H. Sadeghi, C. J. Lambert, A. Narita, K. Müllen, and L. Bogani, Nature **557**, 691 (2018).
[25] A. Rycerz, J. Tworzydło, and C. W. J. Beenakker, Nature Physics **3**, 172 (2007).
[26] N. M. Freitag, T. Reisch, L. A. Chizhova, P. Nemes-Incze, C. Holl, C. R. Woods, R. V. Gorbachev, Y. Cao, A. K. Geim, K. S. Novoselov, J. Burgdörfer, F. Libisch, and M. Morgenstern, Nature Nanotechnology **13**, 392 (2018).
[27] M. Sui, G. Chen, L. Ma, W.-Y. Shan, D. Tian, K. Watanabe, T. Taniguchi, X. Jin, W. Yao, D. Xiao, and Y. Zhang, Nature Physics **11**, 1027 EP (2015).
[28] T. Fujita, M. B. A. Jalil, and S. G. Tan, App. Phys. Lett. **97**, 043508 (2010).
[29] M. M. Grujić, M. Ž. Tadić, and F. M. Peeters, Phys. Rev. Lett. **113**, 046601 (2014).
[30] L. A. Ponomarenko, R. V. Gorbachev, G. L. Yu, D. C. Elias, R. Jalil, A. A. Patel, A. Mishchenko, A. S. Mayorov, A. S. Woods, A. S. Wallbank, M. Mucha-Kruczynski, B. A. Piot, M. Potemski, I. V. Grigorieva, K. S. Novoselov, F. Guinea, F. V. I., and A. K. Geim, Nature **497**, 594 (2013).
[31] L. Chen, L. Guo, Z. Li, H. Zhang, J. Lin, J. Huang, S. Jin, and X. Chen, Scientific Reports **3**, 2599 (2013).
[32] G. Z. Magda, X. Jin, I. Hagymási, P. Vancsó, Z. Osváth, P. Nemes-Incze, C. Hwang, L. Biró, and L. Tapasztó, Nature **514**, 608 (2014).
[33] J. Tuček, K. Holá, A. B. Bourlinos, P. Błoński, A. Bakandritsos, J. Ugolotti, M. Dubecký, F. Karlický, V. Ranc, K. Čépe, M. Otyepka, and R. Zbořil, Nature Communications **8**, 14525 EP (2017).
[34] C. J. O. Verzijl, J. S. Seldenthuis, and J. M. Thijssen, J. Chem. Phys. **138**, 094102 (2013).
[35] A. Georges, G. Kotliar, W. Krauth, and M. Rozenberg, Rev. Mod. Phys. **68**, 13 (1996).
[36] M. Snoek, I. Titvinidze, C. Töke, K. Byczuk, and W. Hofstetter, New J. Phys. **10**, 093008 (2008).
[37] A. Valli, G. Sangiovanni, O. Gunnarsson, A. Toschi, and K. Held, Phys. Rev. Lett. **104**, 246402 (2010).
[38] D. Jacob, K. Haule, and G. Kotliar, Phys. Rev. B **82**, 195115 (2010).
[39] A. Valli, G. Sangiovanni, A. Toschi, and K. Held, Phys. Rev. B **86**, 115418 (2012).
[40] G. Mazza, A. Amaricci, M. Capone, and M. Fabrizio, Phys. Rev. Lett. **117**, 176401 (2016).
[41] M. Schüler, S. Barthel, T. Wehling, M. Karolak, A. Valli, and G. Sangiovanni, Eur. Phys. J. Special Topics **226**, 2615 (2017).
[42] H. Das, G. Sangiovanni, A. Valli, K. Held, and T. Saha-Dasgupta, Phys. Rev. Lett. **107**, 197202 (2011).
[43] A. Valli, H. Das, G. Sangiovanni, T. Saha-Dasgupta, and K. Held, Phys. Rev. B **92**, 115143 (2015).
[44] A. Valli, A. Amaricci, A. Toschi, T.Saha-Dasgupta, K. Held, and M. Capone, Phys. Rev. B **94**, 245146 (2016).
[45] A. Amaricci, A. Valli, G. Sangiovanni, B. Trauzettel, and M. Capone, Phys. Rev. B **98**, 045133 (2018).
[46] A. Amaricci, A. Privitera, and M. Capone, Phys. Rev. A **89**, 053604 (2014).
[47] M. Caffarel and W. Krauth, Phys. Rev. Lett. **72**, 1545 (1994).

[48] M. Capone, L. de' Medici, and A. Georges, Phys. Rev. B **76**, 245116 (2007).
[49] A. H. C. Neto, F. Guinea, N. M. R. Peres, K. S. Novoselov, and A. K. Geim, Rev. Mod. Phys. **81**, 109 (2009).
[50] Y. Meir and N. S. Wingreen, Phys. Rev. Lett. **68**, 2512 (1992).
[51] H. Ness, L. K. Dash, and R. W. Godby, Phys. Rev. B **82**, 085426 (2010).
[52] A. Droghetti and I. Rungger, Phys. Rev. B **95**, 085131 (2017).
[53] R. Landauer, IBM J. Res. Dev. **1**, 223 (1957).
[54] M. Büttiker, Phys. Rev. Lett. **57**, 1761 (1986).
[55] See also the extended discussion in the Supporting Information of Ref. 5, at `https://pubs.acs.org/doi/abs/10.1021/acs.nanolett.8b00459`
[56] J. Fernández-Rossier and J. J. Palacios, Phys. Rev. Lett. **99**, 177204 (2007).
[57] M. Kabir and T. Saha-Dasgupta, Phys. Rev. B **90**, 035403 (2014).
[58] K. G. L. Pedersen, M. Strange, M. .Leijnse, P. Hedegard, G. C. Solomon, and J. Paaske, Phys. Rev. B **90**, 125413 (2014).
[59] G. Giovannetti, P. A. Khomyakov, G. Brocks, P. J.Kelly, and J. van den Brink, Phys. Rev. B **76**, 073103 (2007).
[60] R. Skomski, P. A. Dowben, M. S. Driver, and J. A. Kelber, Mater. Horiz. **1**, 563 (2014).
[61] A. Amaricci, J. C. Budich, M. Capone, B. Trauzettel, and G. Sangiovanni, Phys. Rev. Lett. **114**, 185701 (2015).
[62] C. Lefter, V. Davesne, L. Salmon, G. Molnár, P. Demont, A. Rotaru, and A. Bousseksou, Magnetochemistry **2**, 18 (2016).
[63] D. Liu, N. Iwahara, and L. F. Chibotaru, Phys. Rev. B **97**, 115412 (2018).
[64] P. Rickhaus, J. Wallbank, S. Slizovskiy, R. Pisoni, H. Overweg, Y. Lee, M. Eich, M.-H. Liu, K. Watanabe, T. Taniguchi, T. Ihn, and K. Ensslin, Nano Letters **18**, 6725 (2018).